Table 1 Resolution (measured as full width at half maximum) for 0.5, 1.0 and 2.0 mm pinhole aperture diameters obtained from the line source phantom study, which was reconstructed using OS-EM (five iterations) with the three different resolution recovery methods: no resolution recovery (noRR), multi-ray based resolution recovery (rayRR) and point-spread function-based resolution recovery (psfRR)

	Aperture diameter (mm)		
Algorithm	0.5	1.0	2.0
noRR	1.4	1.6	2.4
rayRR	1.3	1.4	1.3
psfRR	1.2	1.4	1.3

where I_{rod} is the average count in the region of interest (ROI) of the rod and I_{bg} the average count in background ROI. The rod ROIs were circular and had the same diameter as the corresponding rod, whereas each background ROI was annular with inner diameter equal to the diameter of the rod and outer diameter was inner diameter plus 2 mm.

All the acquisitions were performed using 0.5, 1.0 and 2.0 mm pinhole aperture (60° opening angle), 55 mm radius of rotation, 4.3 mm pixel size (128 × 128 matrix), 360° circular orbit and 120 projection angles. In order to avoid centre of rotation shifts the projection data was acquired by rotating the target instead of the detector using the system presented by Zeniya *et al.* [18].

The imaging time per projection angle was selected so that the number of total projection counts was similar in the 0.5, 1.0 and 2.0 mm pinhole aperture studies. The average total projection counts in the line source, Jaszczak and contrast phantom study were 0.9 MCts, 5.2 MCts and 51.8 MCts. The images were reconstructed with the three OS-EM algorithms using eight subsets and five iterations with 0.94 mm voxel size.

Results

Table 1 presents the resolution values after five iterations for the three pinhole apertures and three algorithms. The resolution recovery clearly improves resolution and its effect is more pronounced at larger

Fig. 2

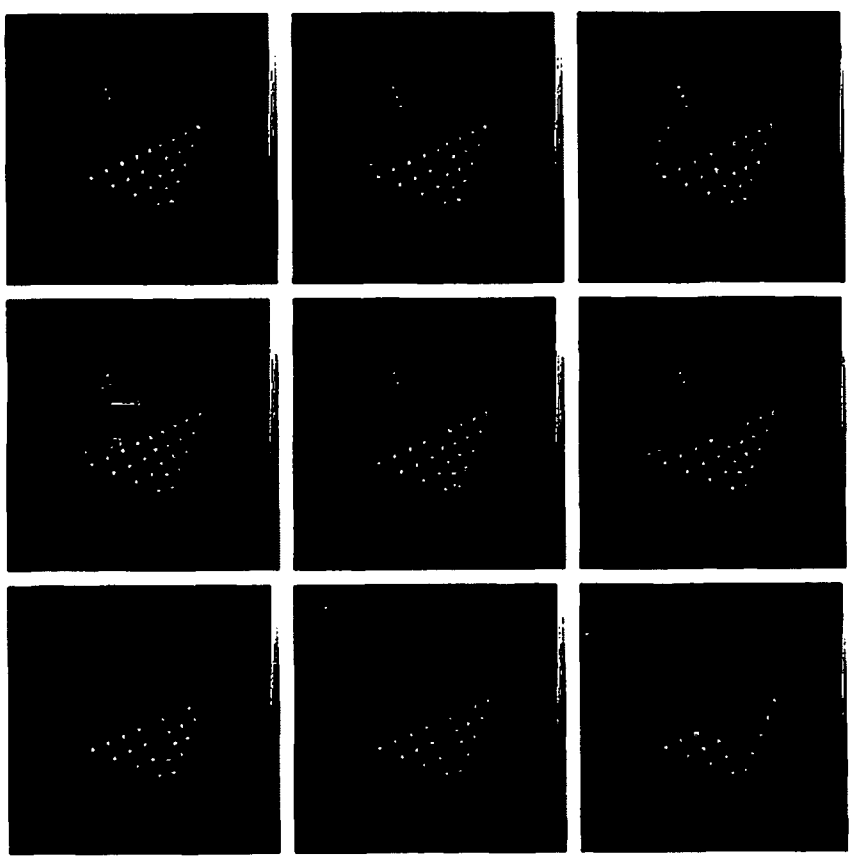

Transverse slices of the Jaszczak phantom study (five slices summed into one); from top to bottom 0.5, 1.0 and 2.0 mm pinhole aperture diameter and from left to right OS-EM with no resolution recovery, multi-ray based resolution recovery and point-spread function based resolution recovery. Air bubbles are marked with arrows on one of the images.

Table 2 Contrast for 0.5, 1.0 and 2.0 mm pinhole aperture diameters obtained from the contrast phantom study reconstructed using OS-EM (five iterations) with the three different resolution recovery methods: no resolution recovery (noRR), multi-ray based resolution recovery (rayRR) and point-spread function based resolution recovery (psfRR)

Rod diameter (mm)	Aperture diameter and resolution recovery method								
	0.5 mm			1.0 mm			2.0 mm		
	noRR	rayRR	psfRR	noRR	rayRR	psfRR	noRR	rayRR	psfRR
2.0	0.34	0.35	0.35	0.29	0.30	0.31	0.13	0.14	0.13
3.0	0.46	0.48	0.50	0.38	0.39	0.41	0.28	0.32	0.28
4.0	0.48	0.49	0.51	0.51	0.54	0.55	0.34	0.40	0.38
5.0	0.48	0.49	0.51	0.49	0.51	0.52	0.37	0.43	0.42
6.0	0.50	0.51	0.53	0.49	0.51	0.53	0.38	0.43	0.41
7.0	0.50	0.50	0.52	0.50	0.53	0.54	0.41	0.46	0.44
8.0	0.49	0.50	0.52	0.48	0.50	0.52	0.39	0.43	0.43
9.0	0.51	0.52	0.53	0.53	0.55	0.57	0.47	0.51	0.49

True contrast of the rods versus background according to Equation 2 is 0.67.

pinhole diameters. On the other hand, the results of the multi-ray and the point-spread function based methods do not differ much. The images of the Jaszczak phantom (Fig. 2) confirm the above findings. The resolution recovery has the biggest effect at the 2 mm pinhole diameter case and the quality of the OS-EM_{rayRR} and OS-EM_{psfRR} images is very similar. The results of the contrast phantom experiment after five iterations are illustrated in Table 2. The methods based on the point-spread function performs slightly better, overall, than does the multi-ray based method.

Discussion

This study compared fast multiple projection ray and analytical point-spread function based resolution recovery methods to uncorrected reconstruction in pinhole SPECT. The multi-ray and point-spread function approaches improved resolution and contrast. The greatest improvement in resolution and contrast was noticed at large pinhole diameters (Tables 1 and 2, Fig. 2). The poor performance of uncorrected reconstruction at larger pinhole diameters is due to the fact that at larger diameters the zero pinhole diameter assumption made in uncorrected reconstruction is violated more than at smaller aperture diameters.

As mentioned in the introduction the biggest problem in incorporating resolution recovery in pinhole SPECT reconstruction is the large computational burden. The calculation time for one iteration of the uncorrected pinhole OS-EM (1.7 GHz Intel processor with 1.0 GB RAM) was 4 min, whereas the computation time for OS-EM_{rayRR} and OS-EM_{psfRR} was 15 min and 10.5 h, respectively, using the acquisition parameters mentioned in the methods section. The reconstruction time of the PSF-based method includes the calculation of the system model, which dominates the calculation time. If the system model for the PSF-based resolution recovery is already stored in a hard disk prior to reconstruction the reconstruction procedure is very fast. Therefore the point-spread function based resolution recovery is suitable for systems where the imaging geometry is fixed [19], because every time the imaging geometry changes, a new system model needs to be generated. The OS-EM_{noRR} and OS-EM_{rayRR}, on the other hand, model the geometry during the reconstruction and can offer clinically acceptable reconstruction times in every case.

The resolution improvement achieved with resolution recovery is important because it allows the use of larger pinhole diameters, which provide higher sensitivity. The poor sensitivity of pinhole collimators has been the biggest problem in small animal pinhole SPECT. Several methods, such as multiple detector heads [3,20] and multiple pinholes [21], have been proposed to overcome this problem, but these approaches require either a multi-headed gamma camera and/or special hardware and are not yet widely applied. Larger injected activities or longer acquisition times are not an optimal approach either, because the radiation burden to the animal or the difficulty of maintaining proper anaesthesia can cause problems. Resolution recovery with a fast resolution recovery algorithm, on the other hand, is almost free of side effects. The only drawback of the multi-ray based approach method is a small increase in noise when compared to reconstruction without resolution recovery, which has been illustrated by Beque *et al.* [16]. The coefficient of variation (COV = standard deviation/mean × 100%) of a large ROI drawn on the uniform background of the contrast phantom also showed this small noise increase. After five iterations the COVs for the 0.5 mm pinhole aperture diameter were 16.1%, 15.4 and 13.7%, when reconstructed with OS-EM_{noRR}, OS-EM_{rayRR} and OS-EM_{psfRR}. The respective values for the 1.0 mm aperture were 16.7%, 17.0% and 14.0%, and 14.6%, 15.9% and 8.4% for the 2.0 mm aperture. The noise properties of the resolution recovery methods were not investigated in detail in this study, because they depended on the implementation of the algorithms. For instance, the noise level of the multi-ray based method

could be decreased by implementing resolution recovery also in the back-projector, but unfortunately this happens at the expense of increased computation time. Noise can also be decreased by using Bayesian reconstruction methods [7], which are almost as fast to execute as the common OS-EM. Therefore from the point of view of the computational burden the best alternative for noise reduction when multi-ray resolution recovery is applied might be to use Bayesian reconstruction methods and model collimator blurring only into the forward projector.

Even though the results presented in this paper were obtained from phantom experiments with activity levels higher than normal can be found in target organs in small animal studies, we are confident that the resolution recovery offers similar improvement in resolution and contrast in small animal studies. However, it is difficult to predict what kind of impact these improvements have, e.g. in brain receptor quantification or measurement of myocardial infarct size in mice and rats. Therefore we plan to further investigate the effect of resolution recovery on (semi-) quantitative values in most frequently used small animal models.

Conclusion

The fast multi-ray resolution recovery method performs almost as well as resolution recovery with accurate point-spread functions and therefore shows promise in improving the resolution–sensitivity trade-off in small animal pinhole SPECT.

Acknowledgement

This work was supported by Japan Society for the Promotion of Science and Nuclear Diagnostics AB.

References

1 Wanet PM, Sand A, Abramovici J. Physical and clinical evaluation of high-resolution thyroid pinhole tomography. *J Nucl Med* 1996; 37:2017–2020.
2 Bahk YW, Chung SK, Park YH, Kim SH, Lee HK. Pinhole SPECT imaging in normal and morbid ankles. *J Nucl Med* 1998; 39:130–139.
3 Acton PD, Choi SR, Plossl K, Kung HF. Quantification of dopamine transporters in the mouse brain using ultra-high resolution single-photon emission tomography. *Eur J Nucl Med Mol Imaging* 2002; 29:691–698.
4 Booij J, de Bruin K, Habraken JBA, Voorn P. Imaging of dopamine transporters in rats using high-resolution pinhole single-photon emission tomography. *Eur J Nucl Med Mol Imaging* 2002; 29:1221–1224.
5 Habraken JBA, de Bruin K, Shehata M, Booij J, Bennink R, van Eck Smit BLF, Busemann Sokole E. Evaluation of high-resolution pinhole SPECT using a small rotating animal. *J Nucl Med* 2001; 42:1863–1869.
6 Scherfler C, Donnemiller E, Schocke M, Dierkes K, Decristoforo C, Oberladstatter M, *et al.* Evaluation of striatal dopamine transporter function in rats by *in vivo* beta-[^{123}I]CIT pinhole SPECT. *Neuroimage* 2002; 17:128–141.
7 Sohlberg A, Lensu S, Jolkkonen J, Tuomisto L, Ruotsalainen U, Kuikka JT. Improving the quality of small animal brain pinhole SPECT imaging by Bayesian reconstruction. *Eur J Nucl Med Mol Imaging* 2004; 31:986–994.
8 Chatziioannou AF. Molecular imaging of small animals with dedicated PET tomographs. *Eur J Nucl Med Mol Imaging* 2002; 29:98–114.
9 Meikle SR, Kench P, Kassiou M, Banati RB. Small animal SPECT and its place in the matrix of molecular imaging technologies. *Phys Med Biol* 2005; 50:R45–R61.
10 Schramm NU, Ebel G, Engeland U, Schurrat T, Béhé M, Behr TM. High-resolution SPECT using multipinhole collimation. *IEEE Trans Nucl Sci* 2003; 50:315–320.
11 Shepp LA, Vardi Y. Maximum likelihood reconstruction for emission tomography. *IEEE Trans Med Imag* 1982; MI-1:113–122.
12 Hudson HM, Larkin RS. Accelerated image reconstruction using ordered subsets of projection data. *IEEE Trans Med Imag* 1994; 13:601–609.
13 Hutton BF, Lau YH. Application of distance-dependent resolution compensation and post-reconstruction filtering for myocardial SPECT. *Phys Med Biol* 1998; 43:1679–1693.
14 Yokoi T, Shinohara H, Onishi H. Performance evaluation of OSEM reconstruction algorithm incorporating three-dimensional distance-dependent resolution compensation for brain SPECT: a simulation study. *Ann Nucl Med* 2002; 16:11–18.
15 Zeng GL, Bai C, Gullberg GT. A projector/backprojector with slice-to-slice blurring for efficient three-dimensional scatter modeling. *IEEE Trans Med Imaging* 1999; 18:722–732.
16 Beque D, Vanhove C, Andreyev A, Nuyts J, Defrise M. *Correction for Imperfect Camera Motion and Resolution Recovery in Pinhole SPECT.* IEEE Nuclear science symposium and medical imaging conference rome, Italy 2004.
17 Metzler SD, Bowsher JE, Greer KL, Jaszczak RJ. Analytic determination of the pinhole collimator's point-spread function and RMS resolution with penetration. *IEEE Trans Med Imag* 2002; 21:878–887.
18 Zeniya T, Watabe H, Aoi T, Kim KM, Teramoto N, Hayashi T, *et al.* A new reconstruction strategy for image improvement in pinhole SPECT. *Eur J Nucl Med Mol Imaging* 2004; 31:1166–1172.
19 Beekman FJ, Vastenhouw B. Design and simulation of a high-resolution stationary SPECT system for small animals. *Phys Med Biol* 2004; 49: 4759–4792.
20 Ishizu K, Mukai T, Yonekura Y, Pagani M, Fujita T, Magata Y, *et al.* Ultra-high resolution SPECT system using four pinhole collimators for small animal studies. *J Nucl Med* 1995; 36:2282–2287.
21 Beekman FJ, van der Have F, Vastenhouw B, van der Linden AJ, van Rijk PP, Burbach JP, *et al.* U-SPECT-I: a novel system for submillimeter-resolution tomography with radiolabeled molecules in mice. *J Nucl Med* 2005; 46:1194–1200.

Annals of Nuclear Medicine Vol. 20, No. 9, 583–588, 2006

PET kinetic analysis—compartmental model

Hiroshi WATABE,* Yoko IKOMA,** Yuichi KIMURA,*** Mika NAGANAWA***,**** and Miho SHIDAHARA**

*Department of Investigative Radiology, National Cardiovascular Center Research Institute
**Department of Biophysics, Molecular Imaging Center, National Institute of Radiological Sciences
***Positron Medical Center, Tokyo Metropolitan Institute of Gerontology
****Japan Society for the Promotion of Science

PET enables not only visualization of the distribution of radiotracer, but also has ability to quantify several biomedical functions. Compartmental model is a basic idea to analyze dynamic PET data. This review describes the principle of the compartmental model and categorizes the techniques and approaches for the compartmental model according to various aspects: model design, experimental design, invasiveness, and mathematical solution. We also discussed advanced applications of the compartmental analysis with PET.

Key words: PET, compartmental model, pharmacokinetics

1. Introduction

RECENTLY, positron emission tomography (PET) imaging with ^{18}F labeled fluorodeoxyglucose (FDG) has shown great success in tumor detection and cancer staging. Furthermore, PET has been widely accepted as a tool for "molecular imaging," which is regarded as the main paradigm for twenty-first century biology.[1–3] Among several imaging modalities (such as MRI, SPECT, optical imaging) for molecular imaging, PET imaging has several advantages such as high sensitivity and ability for quantitative measurement. However, in order to exploit PET's potential fully, one must understand some basic principles behind PET. Data measured by PET camera are composed of various signals. In order to isolate the component of the signal of interest, a mathematical framework has been developed by several investigators. "Compartmental model" originated from the field of pharmacokinetics and is a commonly used mathematical model for analyzing PET data. Many methods to analyze PET data have been developed based on the compartmental model including the quantification of blood flow,[4] cerebral metabolic rate for glucose,[5] cerebral oxygen utilization[6] and neuroreceptor ligand binding.[7] In this review, the concept of the compartmental model with PET is introduced and several applications by the compartmental model and PET are discussed.

Received October 2, 2006, revision accepted October 2, 2006.

For reprint contact: Hiroshi Watabe, Ph.D., Department of Investigative Radiology, National Cardiovascular Center Research Institute, 5–7–1 Fujishiro-dai, Suita, Osaka 565–8565, JAPAN.

E-mail: watabe@ri.ncvc.go.jp

2. General concepts for compartmental model to analyze PET data

In a typical PET study, PET data are sequentially obtained after the radioactive tracer is introduced (usually administrated intravenously) over time. By applying proper corrections for attenuation, dead-time of detector, physical decay of radioactivity and scattered photons, PET data represent the tracer concentration (Bq/m*l*) at a certain time. In order to interpret the observed PET data over time, we assume there are physiologically separate pools of tracer substance as "compartments." Figure 1 represents general four compartments model or three tissue compartments model. The first compartment is the arterial blood. From arterial blood, the radioligand passes into the second compartment, known as the free compartment. The third compartment is the region of specific binding which we are usually interested to observe. The fourth compartment is a nonspecific-binding compartment that exchanges with the free compartment. The transport and binding rates of the tracer (K_1 [m*l*$\cdot$g$^{-1}\cdot$min^{-1}], k_2 [min^{-1}], k_3 [min^{-1}], k_4 [min^{-1}], k_5 [min^{-1}] and k_6 [min^{-1}] in Fig. 1) are assumed to be linearly related

to the concentration differences between two compartments, and the following differential equations are described at time t [min].

$$\frac{dC_b(t)}{dt} = k_3C_f(t) - k_4C_b(t)$$

$$\frac{dC_f(t)}{dt} = K_1C_p(t) + k_6C_n(t) + k_4C_b(t) - (k_2 + k_3 + k_5)C_f(t)$$

$$\frac{dC_n(t)}{dt} = k_5C_f(t) - k_6C_n(t) \qquad (1)$$

where $C_p(t)$, $C_f(t)$, $C_b(t)$ and $C_n(t)$ are radioactivity concentrations at time t [min] for each compartment. Data obtained by PET camera ($C_{PET}(t)$) are a summation of these compartments as

$$C_{PET}(t) = C_f(t) + C_b(t) + C_n(t) \qquad (2)$$

The parameters can be estimated by fitting the model to measured PET data with arterial radioactivity concentration ($C_p(t)$) as input function. The $C_p(t)$ must be measured separately from PET data acquisition. The frequent manual sampling of the arterial blood or continuous radioactivity monitoring by external radiation detector[8,9] is required (there are several techniques to avoid blood sampling, which will be discussed later).

It is sometimes more useful to employ combinations of the parameters as "macro parameter" to represent the observed data rather than individual parameter. The frequently used macro parameters are distribution volume (K_1/k_2), and binding potential ($\frac{K_1k_3}{k_2k_4}$ or $\frac{k_3}{k_4}$). These estimated parameters or the macro parameters provide several useful pieces of information such as the behavior of target molecule, physiological function, and pharmacokinetics.

There are several assumptions that underlay the compartmental model to interpret PET data. Physiological process and molecular interactions are not influenced by injected radioligand and should be constant during PET measurement. Because PET imaging has sensitivity of 10^{-11}–10^{-12} mol/l, most PET studies fulfill this assumption. We presume that each compartment is homogeneous and the radioligand that passes from one compartment to the other is instantaneously mixed in the compartment.

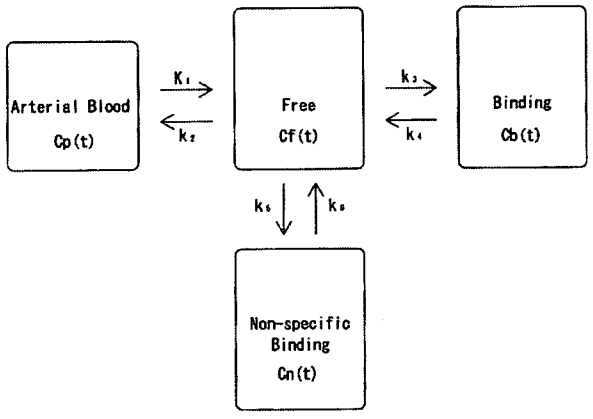

Fig. 1 General three tissue (or four-compartments) compartmental model. This model consists of components of plasma, free ligand in tissue, specific binding and non-specific binding and six rate constants (K_1–k_6).

3. Classification of the compartmental models and analyzes

Many compartmental models and many methods have been proposed to analyze PET data. In this section, we classify the models and methods in different aspects.

3.1 Number of the compartments

The answer for how many compartments must be considered depends on the chemical and biological properties of the radioligand. Moreover, the three tissue compartmental model in Figure 1 has six parameters and the statistical quality of the observed PET data or the statistical properties of the defined model often does not allow to estimate six parameters at once. By reducing the number of the compartments, the number of estimated parameters is reduced and the statistical variability of the parameters is suppressed.

The simplest compartmental model is the model which has only one tissue compartment (Fig. 2). The most popular application of the single-tissue compartment is blood flow measurement by ^{15}O labeled water and PET based on the Fick principle.[4] The single-tissue compartmental model is sometimes enough for many radioligands to describe their kinetics. The neuroreceptor ligand actually behaves under the two or three tissue compartmental model; however, practically one tissue compartmental model is sufficient to describe the kinetics of the ligand in some cases.[10,11]

The two tissue compartmental model (Fig. 3) fits many radioligand tracers well. [^{18}F]FDG is a typical example of the two tissue compartmental model. For many neuroreceptor radioligands, rapid equilibrium between the nonspecific-binding and free compartments can be assumed and the two tissue compartmental model is enough to interpret the kinetics of the ligand.

If the injected radioligand is metabolized and the me-

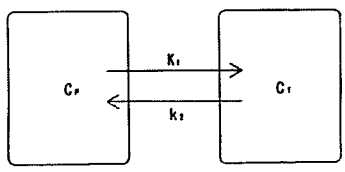

Fig. 2 Single tissue compartmental model. This model has only one compartment in tissue and exchange radiotracer between plasma compartment (C_P) and tissue compartment (C_T) by two rate constants K_1 and k_2.

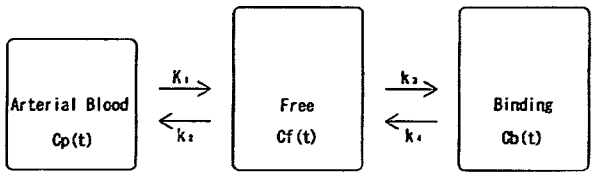

Fig. 3 Two tissue (or three-compartments) compartmental model. This model consists of components of plasma, free ligand (plus non-specific binding) in tissue and specific binding and four rate constants (K_1–k_4).

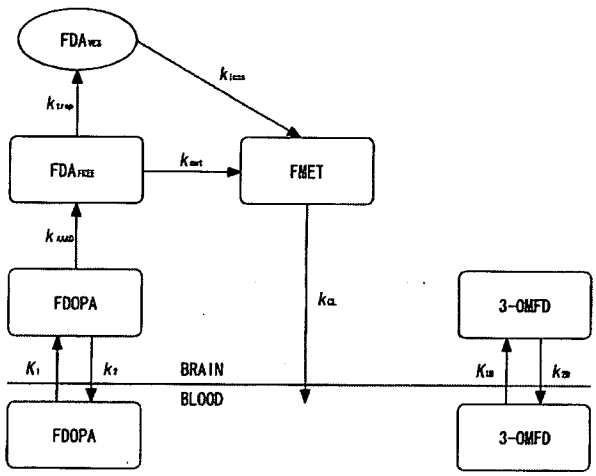

Fig. 4 Compartmental model of FDOPA metabolism.[12] The model consists of FDOPA, fluorodopamine (FDA), FDA metabolites (FMET consist of [^{18}F]6-fluoro-L-3,4-dihydroxyphenylacetic acid, [^{18}F]6-fluorohomovanillic acid) and 3-*O*-methyl-fluorodopa (3-OMFD).

tabolized compounds are detectable by the PET camera, the compartmental model must take into account the kinetics of the metabolites, which results in more compartments and parameters to be estimated. [^{18}F]6-fluoro-L-dopa (FDOPA) is a typical example of these kinds of radioligands (See Fig. 4).[12]

Alternatively, there are several approaches which do not require assumption of the number of compartments. Instead, they estimate the macro parameters such as the distribution volume based on common properties among the compartmental models. Graphical approaches by Patlak et al.[13] and Logan et al.[14] estimate the macro parameter by graphically fitting a straight line to the transformed experimental data. Spectral analysis[15,16] assumes that the observed PET data can be described by sets of exponentials as impulse response function and employs non-negative least squares fitting to estimate exponential basis functions. The spectral analysis also supplies information on the number of compartments. The basis pursuit denosing[17] extends the concept of the spectral analysis and permits negative coefficient for the basis functions, facilitating adaptation for the reference tissue model (see below for explanation of the reference tissue model).

3.2 Bolus or infusion administration of the radiotracer

In many cases, the radiotracer is administrated as a bolus, and dynamic changes of PET data are observed and analyzed. As shown in Eq. 1, the compartmental model mathematically includes differential equations. If equilibrium condition is achieved, i.e. the change rate of the concentration against time in the compartment is zero, the left side of Eq. 1 becomes zero, which simplifies mathematical formulations for the compartmental analysis. Continuously supplying radiotracer may produce equilibrium condition. Well established technique using this strategy is measurements of cerebral blood flow and oxygen consumption by continuous inhalations of ^{15}O–CO, ^{15}O–CO_2 and ^{15}O–O_2 gases.[18] Another example of usage of the equilibrium condition is bolus plus constant infusion paradigm for neuroreceptor study.[19] This experimental paradigm starts with bolus injection of the radiotracer followed by continuously infused administration of the radiotracer to achieve constant concentrations in the tissue and blood. The distribution volume and binding potential can be easily obtained by calculating ratios between the radioactivity concentrations in the tissues and blood. The rate of the infusion may vary between subjects, and optimal scheduling of the experiments must be sought for success of the bolus plus infusion paradigm.[20]

3.3 Compartmental analysis with the arterial input function or without the arterial input function

As described above, the arterial radioactivity curve as the input curve is essential for the compartmental analysis with PET. However, arterial sampling is invasive and technically demanding. If the heart chamber is inside the field-of-view of PET camera, the arterial input function can be directly derived from PET images.[21,22] Or the input function is estimated by extracting components of blood from PET images by means of image-processing.[23,24]

Alternatively, several techniques based on compartmental analysis have been developed. A common strategy for these techniques is omitting the arterial input function by assuming that all pixels of the interest in the PET data share the same arterial input function.[25–28] Many radioligands for neuroreceptor use the reference tissue model (Fig. 5) of Lammertsma et al.[27] or its extensions.[29] Although these techniques have several advantages over the method with the arterial input function, especially non-invasiveness, these techniques generally have more assumptions and need caution for use. For example, the existence of the specific binding in the reference region result in an underestimation of specfic binding in the target region.[30]

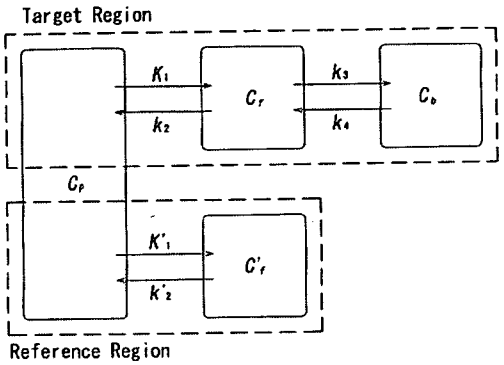

Fig. 5 Reference tissue model.[27] The target region and the reference region have the same plasma input function. It uses the C'_f, time activity curve of the reference region as an indirect input function.

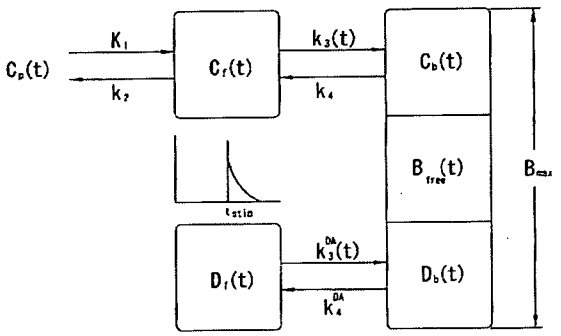

Fig. 6 Extended receptor model which accounts for dopamine competition.[37] Amphetamine is introduced at time t_{stim}, and endogenous dopamine is released. The parameter k_3 is varied according to free receptor B_{free}.

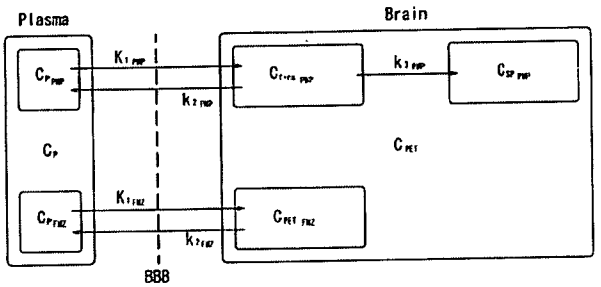

Fig. 7 Combined compartmental model for dual injections of PMP and DTBZ or FMZ.[38]

3.4 Non-linear or linear fitting

In order to estimate parameters from Eqs. 1 and 2, non-linear least squares fitting procedure is required. Generally, the non-linear fitting procedure is computationally expensive. Several graphical approaches[13,14,31,32] are available to make non-linear problems into linear ones, which results in quick estimation of parameters. One must select the proper graphical approach for a particular radiotracer. For instance, Patlak plot[13] must be applied for irreversible tracer and Logan plot[14] for reversible tracer. The statistical bias may be introduced due to noise in PET data, and the improper selection of the graphical approach leads to wrong parameter estimation.[32,33] Basis function approach[34,35] is another major method for linearization. In this approach, non-linear terms of solution for the compartmental model are discretely precalculated within available ranges of the kinetic parameters, which results in a linear system to solve. Although the method is computationally more demanding than the graphical approaches, the method allows determination of the individual kinetic parameters of the model.

4. Advanced applications using the compartmental analysis

As mentioned above, the compartmental model assumes that kinetic parameters are constant during the experiment. By intentionally violating this assumption, however, PET can detect and quantify transient changes in neurotransmitter concentrations.[36] Endres et al.[37] extended the compartmental model to consider endogenous dopamine release (Fig. 6) and showed that PET data were well fitted to the model.

Recently, there has been growing interest in detecting multiple functions simultaneously within the same subject by multiple injections of radiotracer. Koeppe et al.[38] developed a combined compartmental model (Fig. 7) and studied dual injections of [^{11}C]flumazenil (FMZ), *N*-[^{11}C]methylpiperidinyl propionate (PMP) and [^{11}C]dihydrotetrabenazine (DTBZ). Kudomi et al.[39] developed a model which compensates for the background radioactivity from a previously injected radiotracer and computes CBF and $CMRO_2$ from a single PET acquisition with a sequential administration of [^{15}O]O_2 and [^{15}O]H_2O.

As molecular imaging, many trials are currently underway to image reporter gene expression *in vivo* using PET. The compartmental model can play a role to quantify kinetics of the reporter protein. Green et al.[40] showed that the kinetics of ^{18}F-FHBG can be represented by a two-tissue compartmental model, and k_3 is an index of activity of the reporter protein. However, there are still several issues remaining for quantification of therapeutic gene expression[41] and further investigations are required. One particular problem is that the time scale observed by PET may differ from that for gene expression.

5. Conclusion

The compartmental model is a basic concept to quantitatively evaluate PET data. Many techniques based on the compartmental model have been developed as described in this review and one must select the most appropriate technique to analyze one's own PET data. In future, the

compartmental model will play an important role in molecular imaging.

REFERENCES

1. Luker G, Piwnica-Worms D. Molecular imaging *in vivo* with PET and SPECT. *Acad Radiol November* 2001; 8: 4–14.
2. Dobrucki L, Sinusas A. Molecular imaging. A new approach to nuclear cardiology. *Q J Nucl Med Mol Imaging* 2005; 49 (1): 106–115.
3. Weissleder R. Molecular imaging in cancer. *Science* 2006; 312 (5777): 1168–1171.
4. Kety S. The theory and applications of the exchange of inert gas at the lungs and tissues. *Pharmacol Rev* 1951; 3: 3–41.
5. Reivich M, Kuhl D, Wolf A, Greenberg J, Phelps M, Ido T, et al. The [^{18}F]fluorodeoxyglucose method for the measurement of local cerebral glucose utilization in man. *Circ Res* 1979; 44 (1): 127–137.
6. Mintun M, Raichle M, Martin W, Herscovitch P. Brain oxygen utilization measured with O-15 radiotracers and positron emission tomography. *J Nucl Med* 1984; 25 (2): 177–187.
7. Mintun M, Raichle M, Kilbourn M, Wooten G, Welch M. A quantitative model for the *in vivo* assessment of drug binding sites with positron emission tomography. *Ann Neurol* 1984; 15 (3): 217–227.
8. Eriksson L, Holte S, Bohm C, Kesselberg M, Hovander B. Automated blood sampling systems for positron emission tomography. *IEEE Nucl Sci* 1988; 35 (1): 703–707.
9. Kudomi N, Choi E, Yamamoto S, Watabe H, Kim K, Shidahara M, et al. Development of a GSO detector assembly for a continuous blood sampling system. *IEEE Trans Nucl Sci* 2003; 50 (1): 70–73.
10. Koeppe R, Holthoff V, Frey K, Kilbourn M, Kuhl D. Compartmental analysis of [^{11}C]flumazenil kinetics for the estimation of ligand transport rate and receptor distribution using positron emission tomography. *J Cereb Blood Flow Metab* 1991; 11 (5): 735–744.
11. Watabe H, Channing M, Der M, Adams H, Jagoda E, Herscovitch P, et al. Kinetic analysis of the 5-HT2A ligand [^{11}C]MDL 100,907. *J Cereb Blood Flow Metab* 2000; 20 (6): 899–909.
12. Endres C, Endres C, DeJesus O, DeJesus O, Uno H, Uno H, et al. Time profile of cerebral [^{18}F]6-fluoro-L-DOPA metabolites in nonhuman primate: implications for the kinetics of therapeutic L-DOPA. *Front Biosci* 2004; 9: 505–512.
13. Patlak C, Blasberg R. Graphical evaluation of blood-to-brain transfer constants from multiple-time uptake data. Generalizations. *J Cereb Blood Flow Metab* 1985; 5 (4): 584–590.
14. Logan J, Fowler J, Volkow N, Wolf A, Dewey S, Schlyer D, et al. Graphical analysis of reversible radioligand binding from time-activity measurements applied to *N*-[^{11}C]methyl-(–)-cocaine PET studies in human subjects. *J Cereb Blood Flow Metab* 1990; 10 (5): 740–747.
15. Cunningham V, Jones T. Spectral analysis of dynamic PET studies. *J Cereb Blood Flow Metab* 1993; 13 (1): 15–23.
16. Murase K. Spectral analysis: principle and clinical applications. *Ann Nucl Med* 2003; 17 (6): 427–434.
17. Gunn R, Gunn S, Turkheimer F, Aston J, Cunningham V. Positron emission tomography compartmental models: a basis pursuit strategy for kinetic modeling. *J Cereb Blood Flow Metab* 2002; 22 (12): 1425–1439.
18. Lammertsma A, Jones T, Frackowiak R, Lenzi G. A theoretical study of the steady-state model for measuring regional cerebral blood flow and oxygen utilisation using oxygen-15. *J Comput Assist Tomogr* 1981; 5 (4): 544–550.
19. Carson R, Channing M, Blasberg R, Dunn B, Cohen R, Rice K, et al. Comparison of bolus and infusion methods for receptor quantitation: application to [^{18}F]cyclofoxy and positron emission tomography. *J Cereb Blood Flow Metab* 1993; 13 (1): 24–42.
20. Watabe H, Endres C, Breier A, Schmall B, Eckelman W, Carson R. Measurement of dopamine release with continuous infusion of [^{11}C]raclopride: optimization and signal-to-noise considerations. *J Nucl Med* 2000; 41 (3): 522–530.
21. Iida H, Kanno I, Takahashi A, Miura S, Murakami M, Takahashi K, et al. Measurement of absolute myocardial blood flow with $H_2{}^{15}O$ and dynamic positron-emission tomography. Strategy for quantification in relation to the partial-volume effect. *Circulation* 1988; 78 (1): 104–115.
22. Choi Y, Huang S, Hawkins R, Kim J, Kim B, Hoh C, et al. Quantification of myocardial blood flow using ^{13}N-ammonia and PET: comparison of tracer models. *J Nucl Med* 1999; 40 (6): 1045–1055.
23. Watabe H, Channing M, Riddell C, Jousse F, Libutti S, Carrasquillo J, et al. Noninvasive estimation of the aorta input function for measurement of tumor blood flow with [^{15}O]water. *IEEE Trans Med Imaging* 2001; 20 (3): 164–174.
24. Naganawa M, Kimura Y, Ishii K, Oda K, Ishiwata K, Matani A. Extraction of a plasma time-activity curve from dynamic brain PET images based on independent component analysis. *IEEE Trans Biomed Eng* 2005; 52 (2): 201–210.
25. Watabe H, Itoh M, Cunningham V, Lammertsma A, Bloomfield P, Mejia M, et al. Noninvasive quantification of rCBF using positron emission tomography. *J Cereb Blood Flow Metab* 1996; 16 (2): 311–319.
26. Bella ED, Clackdoyle R, Gullberg G. Blind estimation of compartmental model parameters. *Phys Med Biol* 1999; 44 (3): 765–780.
27. Lammertsma A, Bench C, Hume S, Osman S, Gunn K, Brooks D, et al. Comparison of methods for analysis of clinical [^{11}C]raclopride studies. *J Cereb Blood Flow Metab* 1996; 16 (1): 42–52.
28. Lammertsma A, Hume S. Simplified reference tissue model for PET receptor studies. *Neuroimage* 1996; 4 (3 Pt 1): 153–158.
29. Endres C, Bencherif B, Hilton J, Madar I, Frost J. Quantification of brain muopioid receptors with [^{11}C]carfentanil: reference-tissue methods. *Nucl Med Biol* 2003; 30 (2): 177–186.
30. Kropholler MA, Boellaard R, Schuitemaker A, Folkersma H, Berckel BNMV, Lammertsma AA. Evaluation of reference tissue models for the analysis of [^{11}C](R)-PK11195 studies. *J Cereb Blood Flow Metab* 2006.
31. Yokoi T, Iida H, Itoh H, Kanno I. A new graphic plot analysis for cerebral blood flow and partition coefficient with iodine-123-iodoamphetamine and dynamic SPECT

validation studies using oxygen-15-water and PET. *J Nucl Med* 1993; 34 (3): 498–505.
32. Ichise M, Toyama H, Innis R, Carson R. Strategies to improve neuroreceptor parameter estimation by linear regression analysis. *J Cereb Blood Flow Metab* 2002; 22 (10): 1271–1281.
33. Slifstein M, Laruelle M. Effects of statistical noise on graphic analysis of PET neuroreceptor studies. *J Nucl Med* 2000; 41 (12): 2083–2088.
34. Gunn R, Lammertsma A, Hume S, Cunningham V. Parametric imaging of ligand-receptor binding in PET using a simplified reference region model. *Neuroimage* 1997; 6 (4): 279–287.
35. Watabe H, Watabe H, Jino H, Jino H, Kawachi N, Kawachi N, et al. Parametric imaging of myocardial blood flow with ^{15}O-water and PET using the basis function method. *J Nucl Med* 2005; 46 (7): 1219–1224.
36. Breier A, Su T, Saunders R, Carson R, Kolachana B, Bartolomeis de A, et al. Schizophrenia is associated with elevated amphetamine-induced synaptic dopamine concentrations: evidence from a novel positron emission tomography method. *Proc Natl Acad Sci USA* 1997; 94 (6): 2569–2574.
37. Endres C, Kolachana B, Saunders R, Su T, Weinberger D, Breier A, et al. Kinetic modeling of [^{11}C]raclopride: combined PET-microdialysis studies. *J Cereb Blood Flow Metab* 1997; 17 (9): 932–942.
38. Koeppe R, Raffel D, Snyder S, Ficaro E, Kilbourn M, Kuhl D. Dual-[^{11}C]tracer single-acquisition positron emission tomography studies. *J Cereb Blood Flow Metab* 2001; 21 (12): 1480–1492.
39. Kudomi N, Hayashi T, Teramoto N, Watabe H, Kawachi N, Ohta Y, et al. Rapid quantitative measurement of $CMRO_2$ and CBF by dual administration of ^{15}O-labeled oxygen and water during a single PET scan—a validation study and error analysis in anesthetized monkeys. *J Cereb Blood Flow Metab* 2005; 25: 1209–1224.
40. Green L, Nguyen K, Berenji B, Iyer M, Bauer E, Barrio J, et al. A tracer kinetic model for ^{18}F-FHBG for quantitating herpes simplex virus type 1 thymidine kinase reporter gene expression in living animals using PET. *J Nucl Med* 2004; 45 (9): 1560–1570.
41. Richard J, Zhou Z, Chen D, Mintun M, Piwnica-Worms D, Factor P, et al. Quantitation of pulmonary transgene expression with PET imaging. *J Nucl Med* 2004; 45 (4): 644–654.

ORIGINAL ARTICLE

Annals of Nuclear Medicine Vol. 20, No. 3, 189–194, 2006

Performance of list mode data acquisition with ECAT EXACT HR and ECAT EXACT HR+ positron emission scanners

Hiroshi WATABE,* Keiichi MATSUMOTO,** Michio SENDA** and Hidehiro IIDA*

*Department of Investigative Radiology, National Cardiovascular Center Research Institute
**Institute of Biomedical Research and Innovation

Recently, list mode (event-by-event) data acquisition with positron emission tomography (PET) has been widely noticed because list mode acquisition is superior to conventional frame mode data acquisition in terms of (1) higher efficiency of data storage, (2) higher temporal resolution, and (3) higher flexibility of data manipulation. The aim of this study is to investigate the performance of list mode data acquisition with ECAT EXACT HR and HR+ PET scanners (CTI PET Systems) and its feasibility in clinical applications. A cylindrical phantom (16 cm in diameter and length) filled with a ^{11}C solution for the HR and a ^{15}O solution for the HR+ was scanned several times by varying the radioactivity concentration with the list mode and frame mode acquisitions. The scans were also carried out with a septa (2D mode) and without a septa (3D mode) in order to evaluate the effect of the interplane septa on the quality of the list mode data. The acquired list mode data were sorted into a sinogram and reconstructed using a filtered back-projection algorithm. The count rate performance of the list mode data was comparable to that of the frame mode data. However, the list mode acquisition could not be performed when the radioactivity concentration in the field-of-view was high (exceeding 24 kBq/ml for the 3D mode) due to a lack of sufficient transfer speed for sending data from the memory to hard disk. In order to estimate the pixel noise in a reconstructed image, ten replicated data sets were generated from one list mode data. The reconstructed images with the 3D mode had a signal-to-noise ratio that was more than 60% better than that of the image with the 2D mode. The file size of the generated list mode data was also evaluated. In the case of ECAT EXACT HR+ with the 3D list mode, the list mode data with a generated file size of 2.31 Mbytes/s were generated for 37 MBq injections. Our results suggest that careful attention must be paid to the protocol of the list mode data acquisition in order to obtain the highest performance of the PET scanner.

Key words: PET, list mode, frame mode

INTRODUCTION

RECENTLY, list mode (event-by-event) data acquisition with positron emission tomography (PET) has attracted the attention of many investigators from different fields. In the list mode acquisition, every detected event (both prompt and random) including the location of the line of response in the tomograph is recorded. Although list mode acquisition requires more computational power to process data in comparison to conventional frame mode acquisition, it has several advantages such as (1) higher efficiency of data storage, (2) higher temporal resolution and (3) higher flexibility of data manipulation (flexible frame rebinning, flexible for iterative image reconstruction). Further, many clinical benefits can be expected from the list mode acquisition, for example, real-time motion correction[1,2] and improvement of image quality.[3] However, as compared to the conventional frame mode acquisition, several considerations such as reliability and compatibility must be taken into account before applying

Received August 1, 2005, revision accepted December 6, 2005.

For reprint contact: Hiroshi Watabe, Ph.D., Department of Investigative Radiology, National Cardiovascular Center Research Institute, 5–7–1 Fujishiro-dai, Suita, Osaka 565–8565, JAPAN.

E-mail: watabe@ri.ncvc.go.jp

the list mode acquisition for daily clinical routines.

ECAT EXACT HR[4] and ECAT EXACT HR+[5] (CTI/Siemens, Knoxville, TN, USA) are commercially available PET scanners, which are designed for high spatial resolution, and are employed for research as well as clinical purposes. The goal of this study is to evaluate the performance of the list mode acquisition with ECAT EXACT HR and HR+ scanners and investigate the feasibility of the list mode acquisition in clinical applications. We performed a series of scans of a phantom with the list and frame modes. In order to evaluate the effect of interplane septa on the quality of the list mode data, the scans were carried out with a septa (2D mode) and without a septa (3D mode). The performance of the list mode data acquisition was evaluated with respect to count rate performance, noise property, and generated file size.

MATERIALS AND METHODS

Scanner Description

Table 1 shows the system characteristics of the ECAT EXACT HR scanner in comparison to those of the ECAT EXACT HR+ scanner. Both the scanners have a retractable interplane septa and allow scanning in the 2D mode (with septa) as well as the 3D mode (without septa). For the list mode acquisition, the scanners have a memory of 32 Mbytes for the purpose of gate acquisition. The memory is partitioned into two 16 Mbytes buffers that increment, fill, and write to a hard disk alternately.

Phantom Experiments

We performed phantom experiments for the ECAT EXACT HR scanner at the BF Research Institute (Suita, Osaka, Japan) and ECAT EXACT HR+ scanner at the Institute of Biomedical Research and Innovation (Kobe, Hyogo, Japan). Cylindrical phantoms with a diameter and height of 16 cm were employed for the experiments. A radioactive solution was filled in the phantom and a series of scans were performed with the 2D list, 3D list, 2D frame and 3D frame modes (Table 2). For the EXACT HR scanner, a ^{11}C solution was used, and the duration of each scan was 180 s. For the EXACT HR+ scanner, a ^{15}O solution was used, and the duration of each scan was 30 s. The configurations were different because the experiments were carried out in different institutes using their respective isotopes.

Data Analysis

The obtained list mode data were sorted into sinogram data with a system default span and a maximum ring difference for each scanner (Table 1). The image of each scan was reconstructed using a filtered back-projection technique with a 6-mm Gaussian filter. For the 3D data set, FORE (Fourier rebinning)[6] was applied prior to the reconstruction. The matrix sizes of the reconstructed image were 128 × 128 × 47 for the ECAT EXACT HR scanner and 128 × 128 × 63 for the ECAT EXACT HR+ scanner. The voxel sizes of the reconstructed image were 1.6 × 1.6 × 3.1 mm for the ECAT EXACT HR scanner and 1.6 × 1.6 × 2.4 mm for ECAT EXACT HR+ scanner.

Circular ROIs (regions-of-interest) with a diameter of

Table 1 System characteristics of ECAT EXACT HR in comparison with those of ECAT EXACT HR+ scanners

	HR	HR+
detector ring (slice)	24 (47)	32 (63)
crystals/ring	784	576
block detector design	8 × 7	8 × 8
crystal size (mm)	5.9 × 2.9 × 30	4.39 × 4.05 × 30
axial field-of-view (cm)	15.0	15.5
transaxial field-of-view (cm)	51.4	58.3
element number	336	288
number of angle	392	288
default span (2D)	11	15
default span (3D)	7	9
default maximum ring difference (2D)	5	7
default maximum ring difference (3D)	17	22

Table 2 Summary of the scans performed on the phantom

	HR	HR+
	Radioactivity concentration (kBq/ml)	Radioactivity concentration (kBq/ml)
2D list mode	85.9	135*
	56.1	71.2
	49.8	39.9
	19.4	22.4
	12.4	11.7
3D list mode	24.5*	32.7*
	23.6	21.2
	15.2	14.1
	10.1	13.8
		11.3
		7.65
		5.23
		4.19
2D frame mode	38.8	121
	36.6	61.0
	8.05	30.9
		15.6
		11.1
3D frame mode	19.0	50.4
	15.0	25.5
		12.9
		6.54
		3.31

Radioactivity in the cylindrical phantom when a scan was initiated is shown. * indicates that data are incomplete due to the lack of transfer speed for sending data to the hard disk.

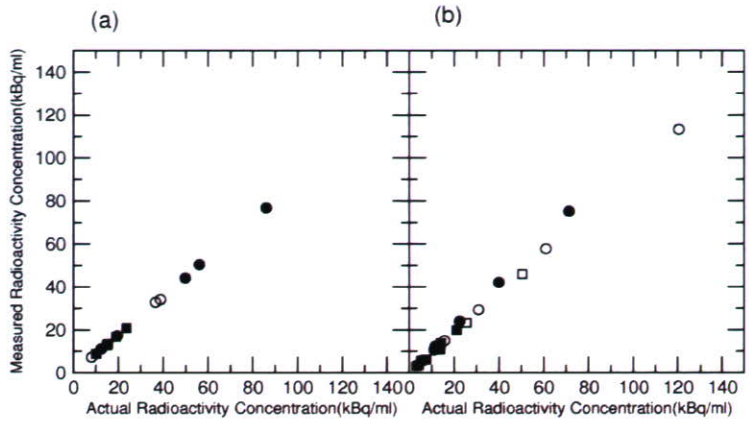

Fig. 1 Comparison of the actual radioactivity concentration inside the phantom and estimated radioactivity concentration from the reconstructed PET image for the ECAT EXACT HR scanner (a) and ECAT EXACT HR+ scanner (b). The filled circles represent the data from the 2D list mode; filled squares, 3D list mode; open circles, 2D frame mode; and open squares, 3D frame mode.

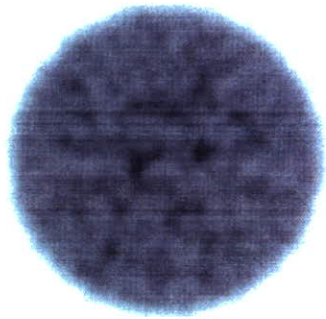

Fig. 2 An example of a generated mean image (*left*) and standard deviation (SD) image (*right*) from 10 replicated data sets generated from one list mode data.

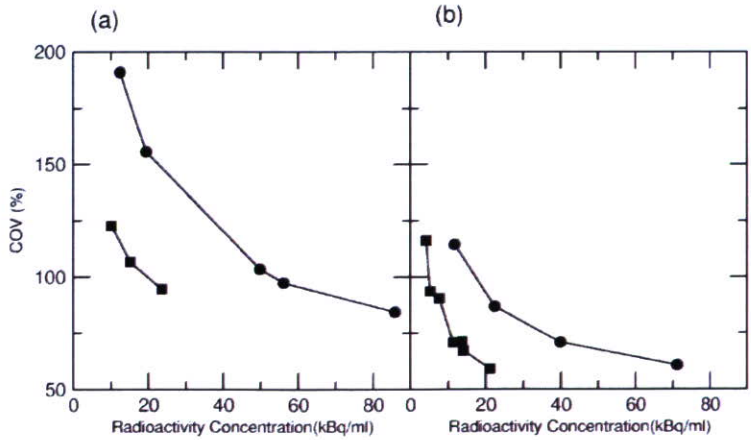

Fig. 3 Relationship between the radioactivity concentration (kBq/ml) and mean coefficient of variance (COV) (%) of the pixel count in the reconstructed image for the ECAT EXACT HR scanner (a) and ECAT EXACT HR+ scanner (b). The lines with filled circles represent the data from the 2D list mode and lines with filled squares represent the data from the 3D list mode.

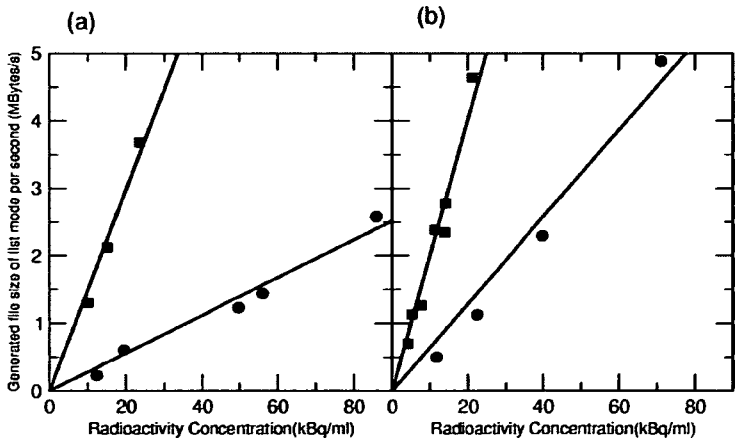

Fig. 4 Relationship between radioactivity concentration (kBq/m*l*) and list mode file size (Mbytes/s) for the ECAT EXACT HR scanner (a) and ECAT EXACT HR+ scanner (b). The filled circles represent the data from the 2D list mode and filled squares represent the data from the 3D list mode. The fitted lines of regression for the data are also shown.

Table 3 Radioactivity concentration in the phantom, NECR (noise equivalent count rate) and COV (coefficient of variance) of the reconstructed image, and the generated list mode file size for the ECAT EXACT HR scanner

Radioactivity concentration (kBq/m*l*)	NECR (/s)	COV (%)	Generated file size per second (Mbytes/s)
	2D list mode		
85.9	9.210×10^4	84.37	2.578
56.1	7.106×10^4	97.32	1.443
49.8	6.423×10^4	103.5	1.234
19.4	4.526×10^4	155.7	0.6034
12.4	1.924×10^4	191.0	0.2279
	3D list mode		
23.6	1.971×10^5	94.57	3.675
15.2	1.465×10^5	106.6	2.123
10.1	1.139×10^5	122.8	1.304

Table 4 Radioactivity concentration in the phantom, NECR and COV of the reconstructed image, and the generated list mode file size for the ECAT EXACT HR+ scanner

Radioactivity concentration (kBq/m*l*)	NECR (/s)	COV(%)	Generated file size per second (Mbytes/s)
	2D list mode		
71.2	1.172×10^5	60.61	4.881
39.9	8.341×10^4	70.73	2.292
22.4	5.470×10^4	86.79	1.124
11.7	3.371×10^4	114.4	0.5012
	3D list mode		
21.2	2.934×10^5	59.05	4.638
14.1	2.331×10^5	67.00	2.779
13.8	1.911×10^5	71.16	2.341
11.3	1.933×10^5	70.76	2.385
7.65	1.214×10^5	90.47	1.263
5.23	1.140×10^5	93.62	1.131
4.19	7.689×10^4	116.1	0.7026

16 cm were placed on the reconstructed image, and the average radioactivity concentration (kBq/m*l*) in the phantom was obtained for each scan.

The NECR (noise equivalent count rate) for each list mode datum was calculated by taking into account the true coincident count rate, random coincident count rate, and scatter fraction in the list mode data.

In order to estimate the noise in a pixel of the reconstructed PET image, 10 replicated data sets were generated from one list mode data. In order to achieve this, the sorting software was modified to produce statistically equivalent multiple sinogram data by splitting the list mode data into pieces. The mean and standard deviation (sd) images were computed from ten reconstructed images. The circular ROIs were placed on both the mean and sd images, and the averaged mean value ($\bar{m}$) and the averaged sd value ($\bar{s}$) were computed. The average COV (coefficient of variance) for each scan was computed from $\bar{m}$ and $\bar{s}$ by considering the physical decay of a radioisotope as follows:

$$\mathrm{COV} = \frac{\bar{s}}{\bar{m}} \cdot \sqrt{\frac{\lambda}{1 - \exp(-\lambda T)}} \times 100\ (\%) \qquad (1)$$

where λ is the physical decay constant (s^{-1}) (0.00567 for ^{15}O and 0.000567 for ^{11}C), and T is the scan duration.

The generated file size of the list mode data per second, S (Mbytes/s), was computed for each list mode scan by considering the physical decay of a radioisotope as follows:

$$S = \frac{F\lambda}{1 - \exp(-\lambda T)} \quad (2)$$

where F (Mbytes) is the generated file size of the list mode data.

RESULTS

Figure 1 (a and b) shows the comparison between the actual radioactivity concentration inside the phantom and the estimated radioactivity concentration from the reconstructed PET image for the ECAT EXACT HR and ECAT EXACT HR+ scanners, respectively. As shown in these figures, there is a good agreement between the list mode data and frame mode data. However, as mentioned in Table 2, if the radioactivity in the field-of-view of the scanner is large, the acquisition of the list mode data would fail due to a lack of sufficient transfer speed for sending data to the hard disk.

Figure 2 shows an example of the generated mean and sd images from the list mode data set. Tables 3 and 4 list the summarized results of the radioactivity concentration in the phantom, NECR and COV in the image, and generated file size of the list mode data for the ECAT EXACT HR and ECAT EXACT HR+ scanners, respectively. Figure 3 shows the relationship between the radioactivity concentration in the phantom and COV in the reconstructed image. As shown in this figure, the image with the 3D acquisition mode has a signal-to-noise ratio that is more than 60% better than that of the image with the 2D acquisition mode. Figure 4 shows the relationship between the radioactivity in the phantom and generated file size of the list mode data. We fitted a line of regression between the radioactivity concentration (A (kBq/ml)) and generated file size (S (Mbytes/s)), and the fitted results are as follows:

$$\begin{aligned} S &= 2.79 \times 10^{-2} \times A \text{ for 2D list mode and ECAT EXACT HR} \\ S &= 1.49 \times 10^{-1} \times A \text{ for 3D list mode and ECAT EXACT HR} \\ S &= 6.43 \times 10^{-2} \times A \text{ for 2D list mode and ECAT EXACT HR+} \\ S &= 2.01 \times 10^{-1} \times A \text{ for 3D list mode and ECAT EXACT HR+} \end{aligned} \quad (3)$$

DISCUSSION

Although the list mode acquisition is not a new technique, the techniques related to the list mode acquisition[3,7–9] have recently become popular due to their advantage as powerful computing systems. Besides the several favorable features of list mode data, additional consideration is required if the list mode acquisition is to be routinely carried out in clinical applications.

Tables 3 and 4 list useful information for scheduling a PET scan with the list mode acquisition. For instance, the injected activity for a patient must be carefully determined by considering 1) the upper limitation of radioactivity concentration, 2) noise in the image and 3) generated file size. The more photons are detected, the larger list mode data are generated. Therefore, generated file size is important from the practical point of view, such as limited size of data storage, time consuming data processes and data backup. According to Eq. (3), assuming that the radioactivity concentration in the field-of-view of the scanner is 10 kBq/ml, a study of ^{15}O for 2 min generates 24.3 Mbytes, 130 Mbytes, 56.0 Mbytes, and 175 Mbytes for the HR 2D list mode, HR 3D list mode, HR+ 2D list mode, and HR+ 3D list mode, respectively. In the case of a ^{11}C study for one hour, 428 Mbytes, 2.29 Gbytes, 987 Mbytes, and 3.01 Gbytes of the list mode data are generated for the HR 2D list mode, HR 3D list mode, HR+ 2D list mode, and HR+ 3D list mode, respectively. In the case of ^{18}F study for one hour, 836 Mbytes, 4.46 Gbytes, 1.93 Gbytes and 6.02 Gbytes for HR 2D list mode, HR 3D list mode, HR+ 2D list mode, HR+ 3D list mode, respectively. The file size of the list mode data for the ECAT EXACT HR+ scanner is larger than that for the ECAT EXACT HR scanner and interestingly the file size of the frame mode for ECAT EXACT HR scanner is larger than that for ECAT EXACT HR+ scanner (sizes of the single-frame sinogram data are 6.2 Mbytes, 23.1 Mbytes, 5.2 Mbytes and 19.8 Mbytes for the HR 2D frame mode, HR 3D frame mode, HR+ 2D frame mode, and HR+ 3D frame mode, respectively).

As shown in Figure 3, the pixel noise in the reconstructed image can be estimated from the list mode data; this is one of the advantages of list mode acquisition. Using multiple frames with very short time duration, the pixel noise can be obtained by the frame mode data. However, it is not ideal due to physical decay of the radioisotope during data acquisition. The pixel noise obtained from the list mode data is quantitatively comparable among scanners. This figure suggests that the noise property of the ECAT EXACT HR+ scanner is superior to that of the ECAT EXACT HR scanner. This is due to the ECAT EXACT HR+ scanner having a higher sensitivity than ECAT EXACT HR scanner, although the two scanners have different system configurations (Table 1). Further, the comparison of the two scanners is complicated.

As shown in Figure 1, the count rate performance of the frame mode and list mode are not surprisingly in good agreement with each other. However, a difference might be observed between the two data sets because of the higher temporal resolution of the list mode data; this enables the accurate correction of the dead-time of the detector and physical decay of the radioisotope. We used the ACS-II (an advanced computational system that is dedicated to handle data from the PET scanner) for both ECAT EXACT HR and HR+ scanners, and the maximum speed of data transfer from the memory to hard disk appears to be approximately 6 Mbytes/s. A read/write controller on the ACS-II with a memory of 32 Mbytes is split into two buffers of approximately 16 Mbytes each.

When the list mode data is being stored from buffer 1 to the hard disk, data are simultaneously written to buffer 2. Once buffer 2 is filled, data are then written to buffer 1, and the data in buffer 2 are written to the hard disk. Since the speed of our hard disk is 6 Mbytes/s and a single event of the list mode data comprises 4 bytes, 1.5 M events/s can be handled. On the other hand, it takes 2.6 s to clear the 16 Mbyte memory. Therefore, if the occurrence of events exceeds 1.5 M events/s, the ACS-II cannot handle all the events.

For usual clinical PET studies, the existence of more than 74 MBq of radioactivity (i.e. 23 kBq/m*l* assuming cylinder with 16 cm diameter) in the field-of-view is not frequent. However, not only true events but also random events are stored in the list mode data and the radioactivity outside the field-of-view must also be considered. It should be noted that since all the possible line of responses are recorded in the list mode data, the number of prompt and random events in the list mode data are greater than those in the frame mode data.

Phantom experiments are often performed with NECR plotted against activity concentration in order to determine the maximum performance of the scanner in terms of image quality. The radioactivity concentrations of about 80 kBq/m*l* and 20 kBq/m*l* give the highest NECR in 2D mode and 3D mode for the ECAT EXACT HR scanner, respectively.[4] These numbers are interestingly close to the maximum radioactivity concentration for the list mode acquisition in our experiments (see Table 2). This suggests the image quality with the list mode can be comparable with that with the frame mode.

In order to use the list mode acquisition at a clinical site, it is also important that a PET scanner be capable of promptly showing the reconstructed PET images. Before reconstruction, a sorting process is necessary for the list mode data, which results in a longer reconstruction time than that for the conventional frame mode data (It takes 0.2 s per 1 M byte of the list mode data for sorting using PC with Xeon CPU (2.4 GHz) and 1 G byte physical memory). Because each event in the list mode data is sequentially stored, it is easy to implement a parallel sorting process. In order to accelerate data processing, the sorting of the list mode data can be performed on a PC cluster[10] which is currently available at a low cost.

The list mode acquisition has several advantages over the conventional frame mode acquisition as mentioned in the first section. However, two disadvantages of the list mode acquisition addressed in this paper, namely, upper limitation of radioactivity and large file size, obstruct the applications of the list mode data on a daily basis. These disadvantages will be overcome along with advances in hardware and software.

CONCLUSION

A series of phantom studies revealed the physical characteristics of the list mode data acquisition with ECAT EXACT HR and HR+ scanners. This study suggests that careful attention must be paid to the protocol of the list mode data acquisition in order to obtain the highest performance of the PET scanner in clinical applications.

ACKNOWLEDGMENT

This study was financially supported by the Budget for Nuclear Research of the Ministry of Education, Culture, Sports, Science and Technology, based on the screening and counseling by the Atomic Energy Commission.

REFERENCES

1. Bloomfield PM, Spinks TJ, Reed J, Schnorr L, Westrip AM, Livieratos L, et al. The design and implementation of a motion correction scheme for neurological PET. *Phys Med Biol* 2003; 48 (8): 959–978.
2. Woo SK, Watabe H, Choi Y, Kim KM, Park CC, Bloomfield PM, et al. Sinogram-based motion correction of PET images using optical motion tracking system and list-mode data acquisition. *IEEE Trans Nucl Sci* 2004; 51 (3): 782–788.
3. Nichols TE, Qi J, Asma E, Leahy RM. Spatiotemporal reconstruction of list-mode PET data. *IEEE Trans Med Imaging* 2002; 21 (4): 396–404.
4. Wienhard K, Dahlbom M, Eriksson L, Michel C, Bruckbauer T, Pietrzyk U, et al. The ECAT EXACT HR: Performance of a new high resolution positron scanner. *J Comput Assist Tomogr* 1994; 18 (1): 110–118.
5. Brix G, Zaers J, Adam LE, Bellemann ME, Ostertag H, Trojan H, et al. Performance evaluation of a whole-body PET scanner using the NEMA protocol national electrical manufacturers association. *J Nucl Med* 1997; 38 (10): 1614–1623.
6. Defrise M, Liu X. A fast rebinning algorithm for 3D positron emission tomography using Johns equation. *Inverse Problems* 1999; 15: 1047–1065.
7. Huesman RH, Klein GJ, Moses WW, Qi J, Reutter BW, Virador PR. List-mode maximum-likelihood reconstruction applied to positron emission mammography (PEM) with irregular sampling. *IEEE Trans Med Imaging* 2000; 19 (5): 532–537.
8. Levkovitz R, Falikman D, Zibulevsky M, Ben-tal A, Nemirovski A. The design and implementation of cosem, an iterative algorithm for fully 3-D listmode data. *IEEE Trans Med Imaging* 2001; 20 (7): 633–642.
9. Byrne C. Likelihood maximization for list-mode emission tomographic image reconstruction. *IEEE Trans Med Imaging* 2001; 20 (10): 1084–1092.
10. Watabe H, Woo Sk, Kim KM, Kudomi N, Iida H. Performance improvement of event-based motion correction for PET using a PC cluster. Conference Record of IEEE Trans Nuclear Science and Medical Imaging Coeference, 2003.

ORIGINAL ARTICLE

Annals of Nuclear Medicine Vol. 20, No. 6, 409–416, 2006

Use of a compact pixellated gamma camera for small animal pinhole SPECT imaging

Tsutomu ZENIYA,* Hiroshi WATABE,* Toshiyuki AOI,* Kyeong Min KIM,** Noboru TERAMOTO,* Takeshi TAKENO,* Yoichiro OHTA,* Takuya HAYASHI,* Hiroyuki MASHINO,*** Toshihiro OTA,*** Seiichi YAMAMOTO**** and Hidehiro IIDA*

*Department of Investigative Radiology, Advanced Medical Engineering Center, National Cardiovascular Center Research Institute
**Nuclear Medicine Laboratory, Radiological and Medical Sciences Research Center, Korea Institute Radiological and Medical Sciences
***Molecular Imaging Laboratory, Inc.
****Department of Electrical Engineering, Kobe City College of Technology

Objectives: Pinhole SPECT which permits *in vivo* high resolution 3D imaging of physiological functions in small animals facilitates objective assessment of pharmaceutical development and regenerative therapy in pre-clinical trials. For handiness and mobility, the miniature size of the SPECT system is useful. We developed a small animal SPECT system based on a compact high-resolution gamma camera fitted to a pinhole collimator and an object-rotating unit. This study was aimed at evaluating the basic performance of the detection system and the feasibility of small animal SPECT imaging. ***Methods:*** The gamma camera consists of a 22 × 22 pixellated scintillator array of 1.8 mm × 1.8 mm × 5 mm NaI(Tl) crystals with 0.2-mm gap between the crystals coupled to a 2″ flat panel position-sensitive photomultiplier tube (Hamamatsu H8500) with 64 channels. The active imaging region of the camera was 43.8 mm × 43.8 mm. Data acquisition is controlled by a personal computer (Microsoft Windows) through the camera controller. Projection data over 360° for SPECT images are obtained by synchronizing with the rotating unit. The knife-edge pinhole collimators made of tungsten are attached on the camera and have 0.5-mm and 1.0-mm apertures. The basic performance of the detection system was evaluated with ^{99m}Tc and ^{201}Tl solutions. Energy resolution, system spatial resolution and linearity of count rate were measured. Rat myocardial perfusion SPECT scans were sequentially performed following intravenous injection of ^{201}TlCl. Projection data were reconstructed using a previously validated pinhole 3D-OSEM method. ***Results:*** The energy resolution at 140 keV was 14.8% using a point source. The system spatial resolutions were 2.8-mm FWHM and 2.5-mm FWHM for ^{99m}Tc and ^{201}Tl line sources, respectively, at 30-mm source distance (magnification factor of 1.3) using a 1.0-mm pinhole. The linearity between the activity and count rate was good up to 10 kcps. In a rat study, the left ventricular walls were clearly visible in all scans. ***Conclusions:*** We developed a compact SPECT system using compact gamma camera for small animals and evaluated basic physical performances. The present system may be of use for quantitation of biological functions such as myocardial blood flow in small animals.

Key words: SPECT, pinhole collimator, compact pixellated gamma camera, small animal

INTRODUCTION

SMALL ANIMAL PET (Positron Emission Tomography) or SPECT (Single Photon Emission Computed Tomography) which permits *in vivo* high resolution three-dimensional (3D) imaging of physiological functions in small

Received February 3, 2006, revision accepted May 10, 2006.
For reprint contact: Tsutomu Zeniya, Ph.D., Department of Investigative Radiology, Advanced Medical Engineering Center, National Cardiovascular Center Research Institute, 5–7–1 Fujishiro-dai, Suita, Osaka 565–8565, JAPAN.
E-mail: zeniya@ri.ncvc.go.jp

laboratory animals, facilitates objective assessment of pharmaceutical development and regenerative therapy in pre-clinical trials.[1–6] Small animal PET has been widely used due to high spatial resolution approaching 1 mm.[7–9] SPECT can also offer high-resolution images by attaching a pinhole collimator with a large magnification factor, when the object is placed close to the pinhole.[10–13] Spatial resolution is improved particularly when a small diameter pinhole is employed.[14–17]

However, a conventional pinhole SPECT has two major limitations. One is its poor sensitivity as compared with small animal PET. The sensitivity of pinhole SPECT is in the order of 1/100–1/1,000 of that of small animal PET, depending on the pinhole diameter, but can be improved by positioning the pinhole collimator close to the object, or by using multiple-detector systems or multiple-pinhole systems.[14,15,17,19,20] Another limitation is the non-uniformity of spatial resolution in the reconstructed 3D images. In pinhole SPECT, the spatial resolution is axially blurred with increased distance from the midplane. This non-uniformity of spatial resolution can be improved by complete data acquisition as demonstrated in our earlier study.[18]

Besides high spatial resolution, the SPECT system has several advantages over PET as its operation is simple, and it does not require an on-site radiochemistry laboratory or a cyclotron for producing radiopharmaceuticals. Pinhole SPECT systems are often composed of clinically used SPECT cameras with pinhole collimator.[3–6,10–15,18,20] However, the clinically used SPECT cameras are inappropriate for small animal imaging, largely due to a lack of manufacturing precision. Also they are not readily accessible to most animal research laboratories.[22]

To overcome these drawbacks, several dedicated small animal pinhole SPECT systems using compact high-resolution gamma cameras have been already developed.[23–25] They used 5″ position-sensitive photomultiplier tube (PSPMT) which had the camera active image region of around 100 mm × 100 mm. In this study, we have employed more a compact pixellated gamma camera with active image region of 43.8 mm × 43.8 mm square coupled to 2″ PSPMT and have developed a compact pinhole SPECT system dedicated to small animal imaging. This study was aimed at evaluating the basic physical performances and the feasibility of small animal imaging in this compact SPECT system.

MATERIALS AND METHODS

Detection system description

The gamma camera consists of a 22 × 22 pixellated scintillator array of 1.8 mm × 1.8 mm × 5 mm NaI(Tl) crystals with 0.2-mm white epoxy gap of diffuse, opaque reflective material between the crystals (Fig. 1 (a)) optically coupled to a 2″ flat PSPMT (Hamamatsu H8500) with 64 channel anodes (Fig. 1 (b)). The scintillator array has a 0.5-mm aluminum window and 2-mm glass window on gamma-ray input and light output sides, respectively. The active imaging region of the camera was 43.8 mm × 43.8 mm square.

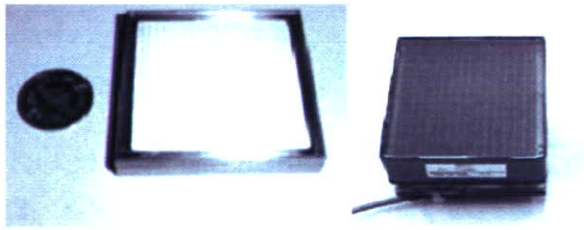

a b

Fig. 1 (a) Photograph of pixellated NaI scintillator array. (b) Photograph of 2-inch flat panel position-sensitive photomultiplier tube.

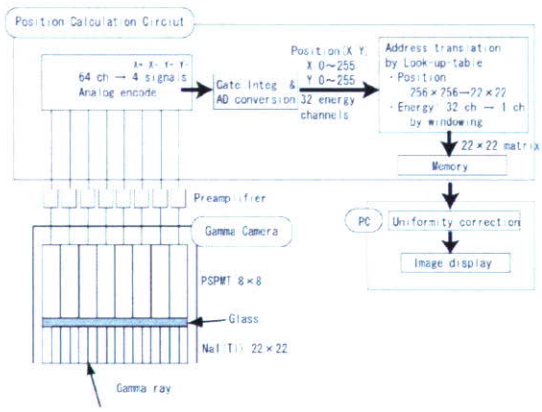

Fig. 2 Schematic diagram of position calculation circuit.

Figure 2 shows a schematic diagram of a position calculation circuit. Analog outputs from 64 PSPMTs through preamplifiers are weighted in proportion to coordinates and are summed in X+, X−, Y+ and Y− directions. After applying gated integration and analog-to-digital conversion for these encoded four analog outputs, the position is obtained by calculating the center of the gravity from the four signals, and is assigned to either pixel in 256 × 256 matrix as a raw image. Also an energy spectrum with 32 channels is collected for each pixel. And then, by address translation using look-up-table (LUT), the raw image of 256 × 256 × 32 matrix is converted to 22 × 22 × 1 image matrix according to the number of scintillators and energy window described below. The counts within the region divided by 22 × 22-matrix grid are summed. The positions of horizontal and vertical lines of the grid are alterable by the interactive tool (Fig. 3) on a personal computer (Windows 2000 (Microsoft)) (PC). Thus, all events are assigned to a 1.8 mm × 1.8 mm crystal in the image matrix. On the other hand, the energy window is set as above and below channel widths from a photopeak

channel searched in each pixel. We assume the use of two radioisotopes of ^{99m}Tc and ^{201}Tl. The main photopeaks are 140 keV and 70 keV for ^{99m}Tc and ^{201}Tl, respectively. Here, the camera gain for ^{201}Tl was set about twice as much as that for ^{99m}Tc. The energy width with each channel corresponds to approximately 10 keV and 5 keV for ^{99m}Tc and ^{201}Tl, respectively. The energy window was actually set at five channels, namely, approximately 36% for both ^{99m}Tc and ^{201}Tl and centered on the photopeak channel searched. Finally, the converted 22 × 22-pixel image is stored on memory and then is transferred to the PC. The PC can perform several tasks such as correcting uniformity, displaying and analyzing images. Figure 3 shows flood raw image by irradiating with a ^{99m}Tc point source. Separation between pixels was well performed except for pixels in columns and rows at the edge. The effective image field-of-view (FOV) that does not enclose the edge pixels was 20 × 20 pixels (or 39.8 mm × 39.8 mm). The resulting image is used as correction matrix to correct for non-uniformity in sensitivity over camera's FOV.

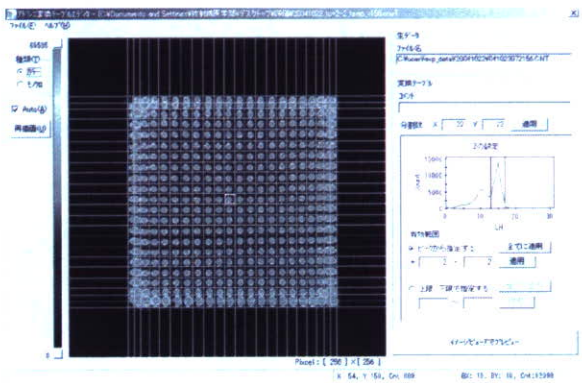

Fig. 3 Interactive tool on PC for making address translation table. The flood raw image was obtained by irradiating with a ^{99m}Tc point source. The separation between pixels was well performed.

Collimator design

As shown in Figures 4 (a) and (b), the pinhole collimator made of tungsten is attached on the gamma camera and has a 0.5-mm or 1.0-mm aperture, 60° opening angle and 39.57-mm focal length. The collimator has a flat face of the single knife-edge pinhole, in order to achieve higher sensitivity and spatial resolution (larger magnification factor) by positioning the pinhole closer to the object. The camera is shielded by tungsten to avoid the penetration of the photon from the surrounding area.

Projection image acquired with the pinhole collimator has non-uniform sensitivity distribution due to the pinhole geometry.[24,25] This non-uniformity can be corrected by using a correction matrix derived from a flood source contained in a thin plate. Figure 4 (c) shows a projection image obtained from the flood source. The correction matrix from this projection image, which has high counts around the center and low counts at the periphery, was actually used to correct the non-uniformity of pinhole sensitivity.

SPECT FOV, namely, the diameter of reconstruction sphere is expressed as:

$$FOV = 2b \sin\left(\frac{\alpha}{2}\right), \tag{1}$$

where b is the distance from the pinhole to the rotation center of the object (radius of rotation: ROR), α is the opening angle of the pinhole collimator. However, when the diameter of the effective image region of camera c_e is shorter than the diameter of the collimator base c, SPECT FOV_e (effective FOV) is expressed as:

$$FOV_e = \frac{c_e}{c} FOV. \tag{2}$$

In this collimator c_e of 39.8 mm is shorter than c of 45.69 mm. Therefore, when b is 30 mm, FOV_e becomes 26.1 mm.

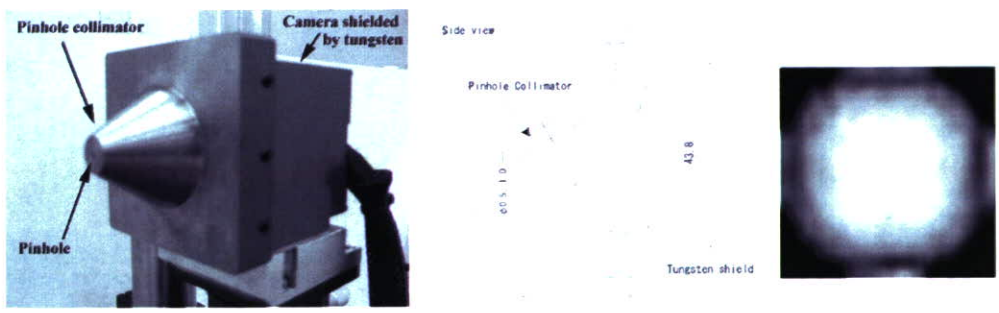

a b c

Fig. 4 (a) Photograph of the pinhole collimator attached to the compact gamma camera. (b) Drawing of side view of the pinhole collimator. (c) Sensitivity map of pinhole collimator. This map was obtained from a flood source filled in a thin plate parallel to the detector and was used to correct non-uniformity of pinhole sensitivity.

SPECT imaging system

Figure 5 shows the pinhole SPECT acquisition system using a compact gamma camera. Data acquisition is controlled by the PC through the camera controller. The rotation of the object stage is synchronized to step and shoot acquisition of the SPECT camera.

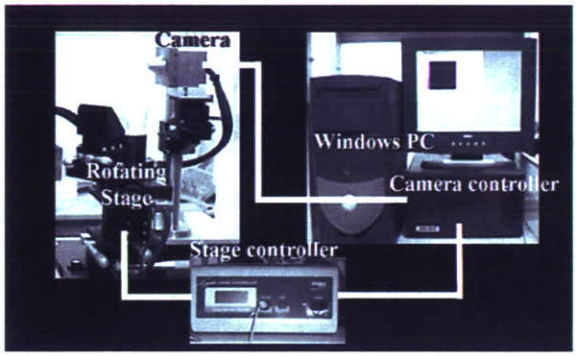

Fig. 5 Pinhole SPECT acquisition system using compact gamma camera. This system consists of compact gamma camera with pinhole collimator, camera controller, PC, object rotating stage and stage controller.

Basic system performances

The performances of the detection system such as the energy resolution, system spatial resolution, sensitivity and linearity of the count rate were examined with ^{99m}Tc (140 keV) and ^{201}Tl (70 keV) sources.

(1) Energy resolution: Energy resolution was measured by uniform irradiation with a 2.18 MBq ^{99m}Tc point source placed at 2 m distant from the camera without the collimator for 12 hours and is defined for each crystal's energy spectrum as full width at half maximum (FWHM) of the photopeak divided by its amplitude. The energy resolution was obtained from an energy spectrum for one crystal near the center of the camera.

(2) System spatial resolution: The FWHMs of the line spread functions (LSFs) were measured in planar image using ^{99m}Tc and ^{201}Tl line sources with 1.14-mm inner diameter placed at 30 mm distant from the 1-mm pinhole. The magnification factor was 1.32. The LSFs of line sources were computed by deconvoluting with rectangular function of 1.14-mm width. The spatial resolutions were defined as the FWHM of Gaussian function obtained from this deconvolution.

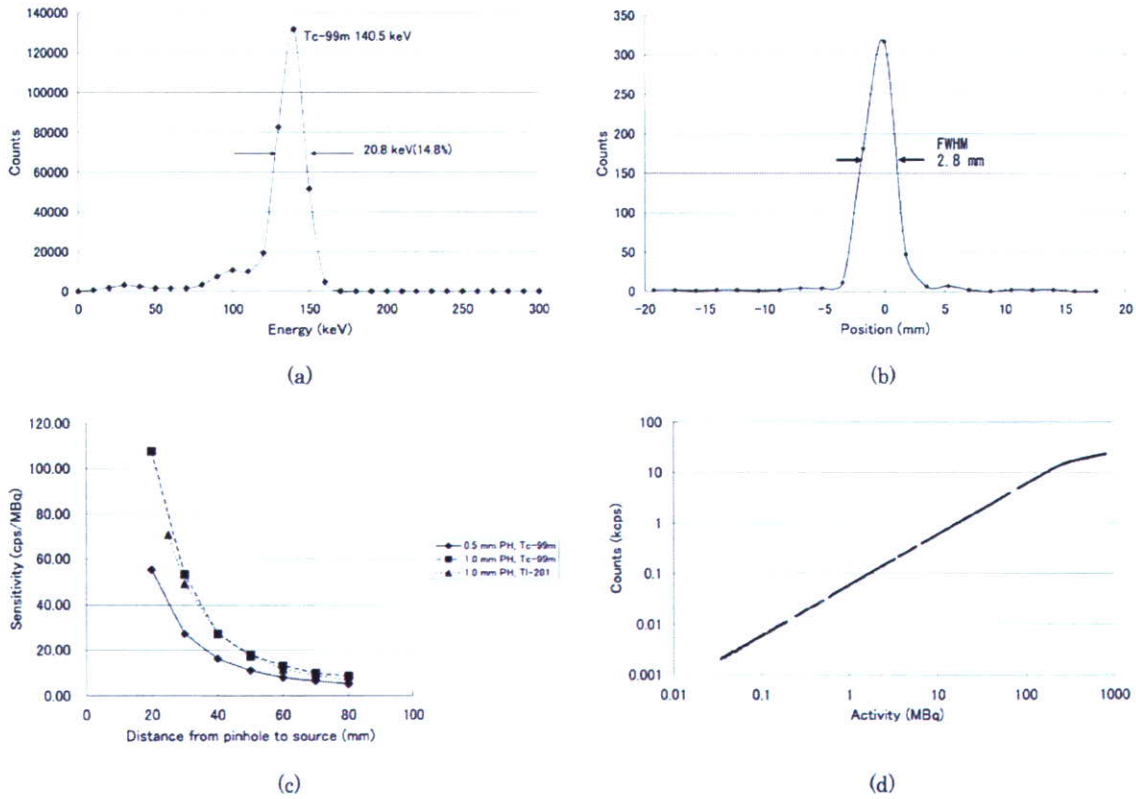

Fig. 6 (a) Energy spectrum obtained from this detection system. The energy resolution was 14.8% FWHM at 140 keV. (b) Planar image profile of 1.14-mm ^{99m}Tc line source. The system spatial resolution obtained from the LSF was 2.8-mm FWHM. (c) On-axis sensitivities for ^{99m}Tc or ^{201}Tl as a function of distance from the pinhole for 0.5-mm or 1.0-mm diameters. (d) Relationship between the source activity and the count rate measured by following decay of ^{99m}Tc source.

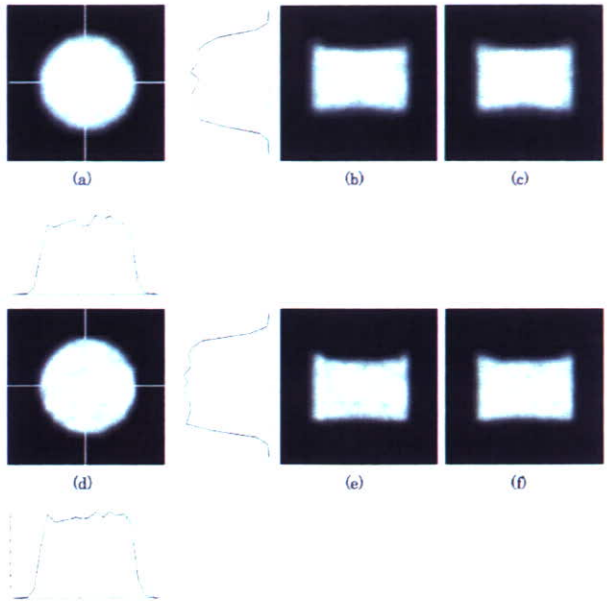

Fig. 7 SPECT images of uniform cylindrical phantom. (a)–(c) are without pinhole sensitivity correction. (d)–(f) are with the correction. (a) and (d) are transverse images. (b) and (e) are coronal images. (c) and (f) are sagittal images. The profiles in the *x* and *y* directions were attached to the transverse images of (a) and (d).

(3) Sensitivity: The system sensitivity on the central axis was measured using a small cylindrical phantom of 0.1 m*l* at eight points in the range from 20 to 80-mm distances with 0.5- or 1.0-mm pinholes and ^{99m}Tc or ^{201}Tl sources.

(4) Linearity of count rate: The counts per 10 min were sequentially measured by following decay of the ^{99m}Tc source. The cylindrical phantom made of glass with 24.3-mm outer diameter and 21.8-mm inner diameter was filled with uniform ^{99m}Tc solution. The center of the phantom was positioned at 30 mm distant from the 1-mm pinhole. Consequently, the relationship between activity and detected counts was examined.

Flood phantom SPECT study

A flood phantom SPECT study was performed to evaluate the uniformity of the reconstruction images. The phantom used in this study was the same one as the cylindrical phantom used to evaluate the linearity of count rate, and was filled with uniform ^{99m}Tc solution. The pinhole collimator with 1-mm diameter was used. The ROR was 30 mm. This resulted in a magnification factor of 1.32. Projection data of 120 views were acquired over 360° using step and shoot acquisition; 10 sec/step, 3° increments. Decay correction and the above-mentioned pinhole sensitivity correction were applied for projection data before reconstruction. The projection data were reconstructed using our previously validated pinhole 3D-OSEM method employing a 3D voxel-driven projector in both back- and forward-projections with eight subsets and two iterations. The corrections for attenuation, scatter and penetration were not done.

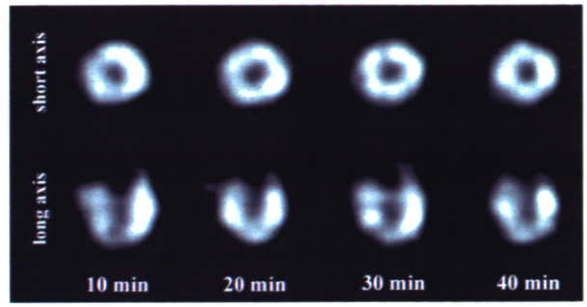

Fig. 8 Short- and long-axial images of rat myocardial perfusion obtained by sequential SPECT scans. The left ventricular walls and cavities were clearly visible in all of four frames obtained for 40 min.

Animal SPECT study

Rat myocardial perfusion SPECT scans were sequentially performed. A male rat weighing 220 g was anesthetized with sodium pentobarbital and held vertically on the object rotating stage, and then was scanned after intravenous 2-min administration of 6.21 MBq/1.5 m*l* ^{201}TlCl into the tail vein. The pinhole of 1 mm was used. The ROR was 30 mm. Scans for 10 min were sequentially performed four times using 360° step and shoot acquisition; 5 sec/step, 3° increments. Like the flood phantom study, projection data were reconstructed using our pinhole 3D-OSEM method with eight subsets and two iterations. Corrections for attenuation, scatter, penetration and pinhole sensitivity were not performed.

RESULTS

Basic system performances

(1) Energy resolution: Figure 6 (a) shows a sample energy spectrum from one crystal near the center of the detector block. The energy resolution was 20.8-keV (14.8%) FWHM at 140 keV.

(2) System spatial resolution: Figure 6 (b) shows a planar image profile of the ^{99m}Tc line source. The spatial resolutions were 2.8-mm FWHM and 2.5-mm FWHM for ^{99m}Tc and ^{201}Tl, respectively.

(3) Sensitivity: Figure 6 (c) shows system sensitivity on the central axis as a function of distance from the pinhole for ^{99m}Tc with 0.5- and 1.0-mm pinholes and for ^{201}Tl with 1.0-mm pinhole. The sensitivity of ^{201}Tl was slightly smaller than that of ^{99m}Tc. In the case of ^{99m}Tc, the sensitivities at a pinhole-source distance of 30 mm were 27.0 and 53.0 cps/MBq with 0.5-mm and 1.0-mm pinholes, respectively. In the case of ^{201}Tl, the sensitivity at the same distance was 49.1 cps/MBq with the 1.0-mm pinhole.